Electronic Supplementary Information

The Effect of the Gas-Solid Contacting Pattern in a High-Temperature Thermochemical Energy Storage on the Performance of a Concentrated Solar Power Plant

S. Ströhle,[a] A. Haselbacher,[b,c] Z. R. Jovanovic[b] and A. Steinfeld[b]
[a] Solar Technology Laboratory, Paul Scherrer Institute, 5232 Villigen, Switzerland
[b] Department of Mechanical and Process Engineering, ETH Zurich, 8092 Zurich, Switzerland
[c] Corresponding author: haselbac@ethz.ch

Contents

Reaction Model and Material Properties

The theoretical equilibrium temperatures of the manganese oxide redox system were calculated with *HSC Chemistry* (www.hsc-chemistry.net) as a function of the oxygen partial pressure.[1] Least-squares fitting of the results gave

$$\ln\left(p_{O_2,eq}\right) = \frac{-21650}{T_{eq}} + 29.744 \tag{1}$$

where $p_{O_2,eq}$ is the equilibrium partial pressure of oxygen in the O_2-N_2 gas mixture corresponding to the equilibrium temperature T_{eq}. The rms of the relative error is 1.2×10^{-3}.

The empirical reaction kinetics model was derived from experimental data obtained with a differential packed bed at various temperatures and oxygen partial pressures.[1,2] The bed consisted of a mixture of commercial Mn_3O_4 powder (Sigma Aldrich, "Manganese (II,III) oxide", CAS: 1317-35-7) with a measured mean particle diameter of $5.5\ \mu m$ and inert SiO_2 (Merck, "Seesand reinst", CAS: 7631-86-9) that was sieved to particle diameters of $200-300\ \mu m$. The ratio of SiO_2 to Mn_3O_4 by mass was at least 40. Each experiment was performed at nearly constant temperature ($\pm5\ K$) and oxygen partial pressure ($p_{O2,out} / p_{O2,in} = 1\pm0.05$). The model is

$$\frac{dX_s}{dt} = k_0 \exp\left(-\frac{E_A}{RT}\right) X_s^{\,a}\left(1-X_s\right)^b \left|1-\frac{p_{O_2}}{p_{O_2,eq}}\right|^s \tag{2}$$

where X_s is the solid conversion ($X_s = 0$ and 1 correspond to fully oxidized and reduced states, respectively), t is time, k_0 is the rate constant, E_A is the apparent activation energy, R is the universal gas constant, T is the temperature, p_{O_2} is the partial pressure of oxygen, $p_{O_2,eq}$ is the equilibrium oxygen partial pressure at the given temperature (see Eq. (1)), and a, b and s are parameters. Note that this model is based on the assumption that the manganese oxides can be completely reduced/oxidized using cycle-independent kinetics, i.e., both the degree of conversion and the kinetics do not change with the number of cycles. The values of the fitting parameters for oxidation and reduction are listed in Tab. 1. The sign of k_0 was chosen to make the conversion rate negative for oxidation and positive for reduction. The maximum conversion rates occur at $X_s = 0.615$ and 0.238 for oxidation and reduction, respectively.

Table 1: Fitted parameters for empirical kinetics model given by Eq. (2)

	Oxidation	Reduction
k_0	$-2.8089\times10^{12}\ s^{-1}$	$8.2167\times10^{9}\ s^{-1}$
E_A	$2.9970\times10^{5}\ J/mol$	$2.5040\times10^{5}\ J/mol$
a	1.0245	0.45633
b	0.64231	1.4584
s	1.3676	20.0

Figure 1 shows the maximum conversion rates obtained from Eqs. (1) and (2) as a function of the temperature and oxygen partial pressure. At a given oxygen partial pressure, an increase in the temperature up to about 1000 K leads to increasing oxidation rates because of the Arrhenius term in Eq. (2). By further increasing the temperature, equilibrium is approached, and the oxidation rate becomes slower because of the pressure term in Eq. (2). To reduce the material, it needs to be heated to a temperature significantly above the theoretical equilibrium temperature. An increase in p_{O_2} leads to a higher equilibrium temperature T_{eq} (see Eq. (1)), and generally causes higher oxidation rates and lower reduction rates at a given temperature.

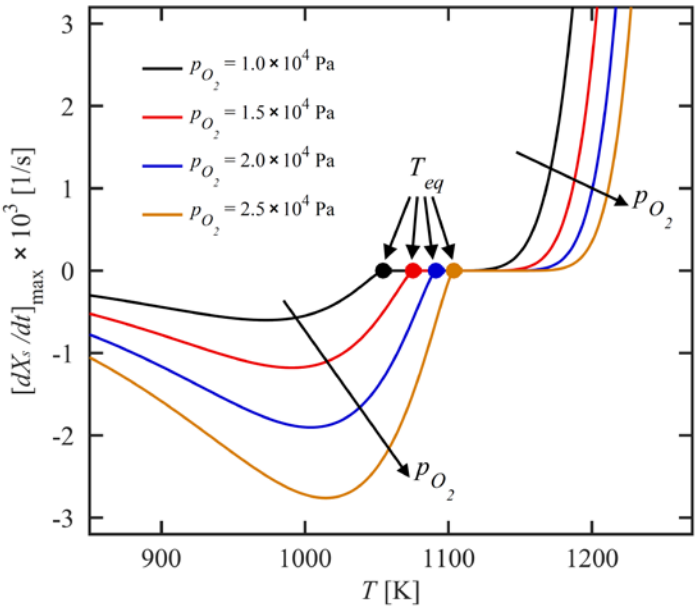

Figure 1: Maximum conversion rate as a function of temperature and oxygen partial pressure determined from Eqs. (1) and (2). The circles indicate the theoretical equilibrium temperatures corresponding to the four oxygen partial pressures.

The theoretical relative mass gain during the oxidation is $\Delta w_{theor,ox} = 0.0349$. We assumed a particle internal porosity of $\varepsilon_p = 0.5$ and an intrinsic density of $\rho_{Mn_3O_4} = 4856\, kg/m^3$.[3] The heat capacities of the manganese oxides were considered to be temperature-dependent.[4] The reaction enthalpy ΔH_{rxn} was calculated as a temperature-dependent function using Kirchhoff's law[5]

$$\Delta H_{rxn}(T) = \Delta H^0_{rxn} + \int_{T^0}^{T} \left[\sum_{products} (\upsilon c_p) - \sum_{reactants} (\upsilon c_p) \right] dT \qquad (3)$$

where the superscript ^{0} denotes standard conditions and υ is the stoichiometric coefficient.

For the simulations of the fluidized bed, the particle size (100 μm) was chosen to represent Geldart A type particles that are typically used in industrial fluidized beds.[6] The particles were considered to be small enough so that the temperature and reaction rate

within each particle could be assumed to be uniform. Therefore, Eq. (2) was used to calculate the reaction rates.

The size of granules used for the simulations of the packed bed TCS ($5\,mm$) is typical for packings in large-scale industrial packed beds.[7] Granules of such a diameter result in small to moderate pressure drops for typical packed-bed lengths. Eq. (2) was evaluated in each cell of a granule as a function of the local values of T, p_{O_2}, and X_s. The effective thermal conductivity of Mn_3O_4 powder was measured as $k_{g,eff} = 0.59\,W/mK$.[8] Simulations indicated that varying the effective intragranule thermal conductivity within the range of $0.01-1\,W/mK$ did not lead to significant intragranule temperature gradients. However, varying $k_{g,eff}$ in the given range was found to affect the effective axial bed conductivity and therefore the axial gas and solid phase temperature profiles. In principle, the flattening of the axial temperature profiles through increasing $k_{g,eff}$ could lead to an increase in $T_{f,c,out}$, and therefore to a reduction in the effective gravimetric storage density $\tilde{e}_{tot}$. However, for the range of $0.01-1\,W/mK$ the maximum difference in $T_{f,c,out}$ was about $1\,K$, and the corresponding relative change in $\tilde{e}_{tot}$ was less than 1%.

The effective mass diffusion coefficient was set to $D_{g,eff} = 10^{-5}\,m^2/s$ following simulations that showed variations in the range of $10^{-6}-10^{-3}\,m^2/s$ to have a negligible influence on the reaction rates.

The density of air was calculated from the ideal gas law. The variation of the heat capacity $c_{p,air}$ with the temperature was based on tabulated values of pure nitrogen and oxygen at $1\,bar$.[9]

Effect of Packed Bed Reactor Length and Granule Size

The reason for choosing a length of $L_{bed} = 1.5\,m$ for the packed bed may not be clear at first sight. In fact, one may expect a shorter bed to be advantageous because almost no energy is stored in the granules near the cold end of the bed (see $1.0\,m < z < 1.5\,m$ in Fig. 9 in the manuscript). However, a reduction in the bed length not only affects the gravimetric energy storage density ($\tilde{e}_{tot}$) but also the maximum HTF outflow temperature during charging ($T_{f,c,out,max}$). From the results of additional simulations for different bed lengths, provided in Tab. 2, it can be seen that a reduction in the bed length would lead to an increase in $\tilde{e}_{tot}$ at the expense of increased $T_{f,c,out,max}$. As stated in Section 3 of the manuscript, in a parallel configuration a deviation of $T_{f,c,out}$ from $T_{PB,out}$ leads to exergy losses due to mixing of the HTF streams leaving the TCS and the power block. This is why we have chosen the bed length and operating conditions such that $T_{f,c,out} \approx T_{PB,out}$ during the entire charging period. For specific CSP plant configurations, a limited deviation of $T_{f,c,out}$ from $T_{PB,out}$ may be acceptable because the increased $\tilde{e}_{tot}$ and the associated reduced costs of the TCS material and reactor housing may outweigh the increased exergy losses. Therefore, the conditions resulting in $T_{f,c,out} \approx T_{PB,out}$ lead to conservative results that are more generally applicable.

Table 2: Simulated impact of bed length on the maximum HTF outflow temperature during charging ($T_{f,c,out,max}$) and the gravimetric energy storage density ($\tilde{e}_{tot}$). Note that the remaining parameters were unchanged.

$L_{bed}\,[m]$	$T_{f,c,out,max}\,[K]$	$\tilde{e}_{tot}\,[MJ/kg_{Mn_2O_3}]$
1.5	373	0.334
1.4	373	0.357
1.3	374	0.384
1.2	377	0.416
1.1	386	0.454
1.0	409	0.499

To investigate the sensitivity of our results to the size of the granules, we performed additional simulations for granules of $d_p = 2\,mm$ while keeping the other parameters unchanged. The performance of this packed bed is compared with the performance of the bed packed with $d_p = 5\,mm$ granules in Figs. 2 to 5. The consequences of reducing the granule size can be summarized as follows:

1. The HTF outflow temperature is not affected significantly, see Fig. 2. The drop in $T_{f,d,out}$ at the end of discharging is slightly steeper for the smaller granules but this could be mitigated by a slight decrease in the HTF mass flux during discharging.
2. As shown by Figs. 3 and 4, the axial temperature gradients are steeper for the smaller granules during both charging and discharging. The main reason for the steeper temperature gradients is the increased specific surface area of the granules, which results in enhanced interphase heat transfer. As a result of the

steeper axial temperature profiles, however, as shown by Fig. 5, the *local* gravimetric energy storage density changes slightly: in the bed of $2\ mm$ granules more sensible heat is stored in the reaction zone and less sensible heat is stored in the cooling zone. Figures 3-5 further indicate that the length of the bed of $2\ mm$ granules could be reduced, resulting in increased overall gravimetric energy storage density.

3. A decrease in the granule size leads to an increase in the overall bed pressure drop from $1.5-5.5\ mbar$ ($d_p = 5\ mm$) to $7.9-30.8\ mbar$ ($d_p = 2\ mm$). The corresponding increase in the required pumping work translates to an increase in the parasitic losses from $0.2\,\%$ to $1.1\,\%$ of the energy stored during charging.

From these results it can be concluded that a change in the granule size does not affect any of our key conclusions in Sections 3 to 5.

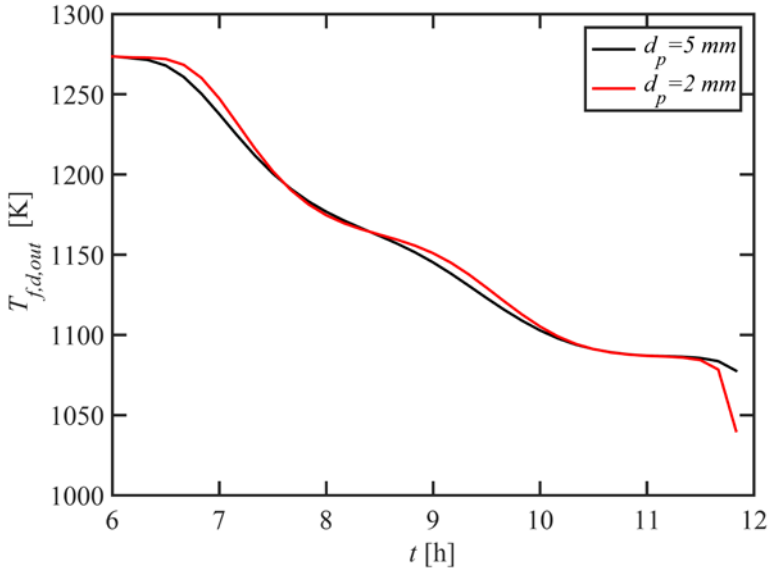

Figure 2: Air outflow temperature during discharging for granule sizes of $5\ mm$ (black line) and $2\ mm$ (red line).

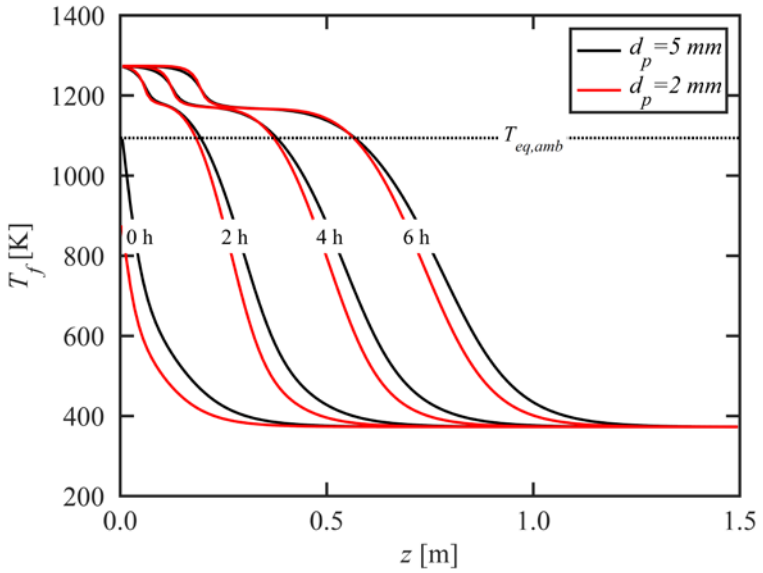

Figure 3: Air temperature in the packed bed as a function of the axial position during charging for granule sizes of $5\ mm$ (black lines) and $2\ mm$ (red lines).

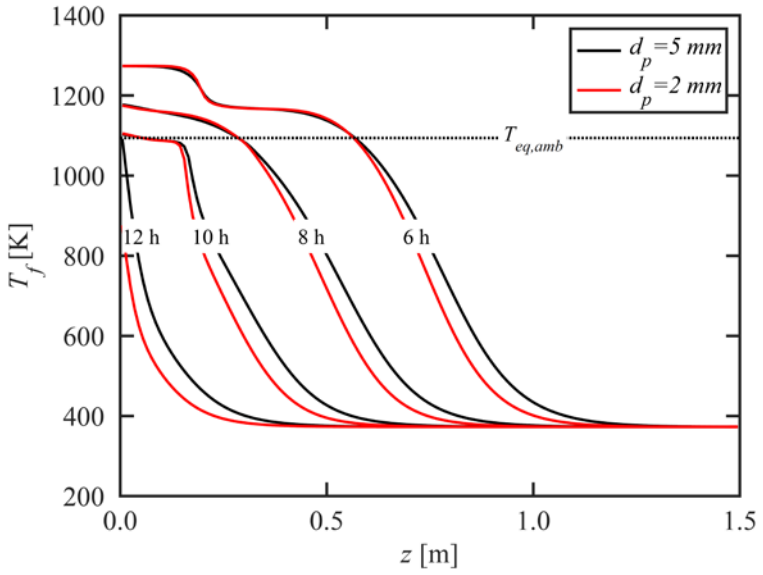

Figure 4: Air temperature in the packed bed as a function of the axial position during discharging for granule sizes of $5\ mm$ (black lines) and $2\ mm$ (red lines).

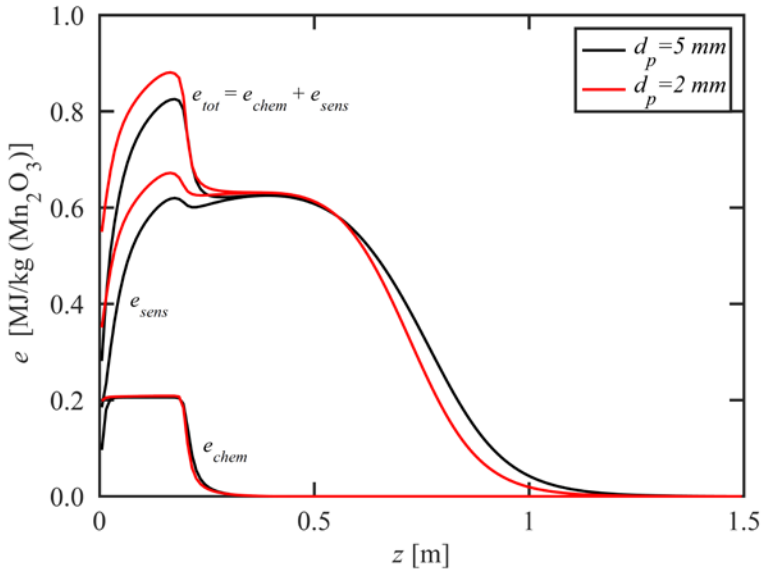

Figure 5: Local gravimetric energy storage density in the packed bed, calculated from the difference in the energy content of the manganese oxide granules between the charged and discharged states for granule sizes of $5\ mm$ (black lines) and $2\ mm$ (red lines).

Fluidized Bed Model

The simulations of the fluidized bed were based on the assumption that the gas reaches the temperature of the solids before leaving the bed. This represents the ideal operating condition for a fluidized-bed TCS that is integrated in a serial configuration. If $T_{f,c,out} > T_s$ during charging, less thermal energy is stored and the attainable discharging duration is reduced. If $T_{f,d,out} < T_s$ during discharging, the thermal efficiency in the power block is decreased. In the following, the conditions under which $T_{f,out} - T_s$ can be considered to be small will be discussed.

If the solid phase is assumed to be perfectly mixed, its temperature can be taken to be spatially uniform. If in addition the temperature of the solid phase is constant in time and plug-flow conditions exist, the energy balance reduces to[6]

$$\frac{L_{bed}}{T_s - T_f}\frac{dT_f}{dz} = \alpha_h \tag{4}$$

where L_{bed} is the bed height, T_s and T_f are the temperatures of the solid and gas phases, respectively, z is the axial coordinate, and α_h is the ratio of interphase heat transfer to the convective heat transport in the bed,

$$\alpha_h = \frac{6(1-\varepsilon_{bed})}{\phi_s}\frac{h_{bed}}{\rho_f u_f c_{p,f}}\frac{L_{bed}}{d_p} \tag{5}$$

where ε_{bed} is the bed void fraction, ϕ_s is the sphericity of the particles, h_{bed} is the apparent heat transfer coefficient between the gas and the bed of solids based on the total surface area of the particles, ρ_f, u_f and $c_{p,f}$ are the density, superficial velocity, and heat capacity of the gas, respectively, and d_p is the particle diameter. The effect of bypassing, i.e., gas rising within bubbles and thus not exchanging heat with the solid phase, can be modeled by a fraction $0 \le \beta \le 1$ of the mass flow of the gas passing through the bed and retaining its inflow temperature. Assuming the remaining mass flow to pass through the bed at plug-flow conditions, and that α_h and β are constants, the gas outflow temperature is given by

$$\frac{T_{f,out} - T_s}{T_{f,in} - T_s} = (1-\beta)\exp(-\alpha_h) + \beta \tag{6}$$

Deviations from plug flow, for example through backmixing of the gas phase, lead to increased differences between the temperature of the gas phase at the outlet and the temperature of the solid phase[6,10,11] and should therefore be avoided. In the limit of a perfectly mixed gas phase,

$$\frac{T_{f,out} - T_s}{T_{f,in} - T_s} = \frac{1}{1+\alpha_h} \tag{7}$$

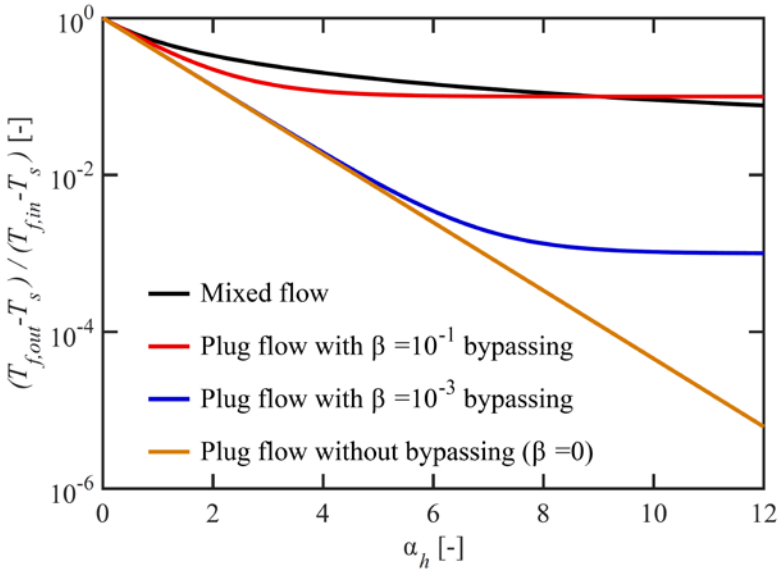

Figure 6: Effect of the gas flow pattern on the fluid outlet temperature in a fluidized bed, assuming that the perfectly mixed solids are kept at a constant temperature.

Equations (6) and (7) are plotted in Fig. 6, from which the following conclusions are drawn. First, for a given value of α_h, plug flow without gas bypassing is the ideal flow pattern in a fluidized bed TCS as it leads to the smallest temperature differences between the solids and the gas at the outlet. Any gas bypassing is detrimental to the heat exchange. For example, for $T_{f,in} = 100\,°C$ and $T_s = 900\,°C$, 10 % gas bypassing leads to $T_s - T_{f,out} \geq 80\,°C$. Second, to reduce the temperature difference at the outlet, the bed should be designed and operated such that α_h is sufficiently large, for example by choosing small particles and large bed heights. Therefore, operating regimes with bubbles causing significant gas bypassing should be avoided for TCS in fluidized beds.[11]

In the simulations presented in this paper, it was assumed that plug flow conditions exist, gas bypassing is avoided, and α_h is large enough such that $T_{f,out} = T_s$ is an accurate approximation. With these assumptions and considering the solids to be at a spatially uniform temperature, the energy equation of the solid phase becomes:

$$\left(1-\varepsilon_{bed}\right)\left(1-\varepsilon_p\right)\rho_s c_s \frac{dT_s}{dt} = \dot{Q}_{rxn} - \dot{Q}_{s\to f} \tag{8}$$

where ε_p is the particle internal porosity, ρ_s and c_s are the intrinsic material density and heat capacity of the solid phase, respectively, $\dot{Q}_{rxn}$ is the heat released by the time-dependent gas-solid reaction, and $\dot{Q}_{s\to f}$ is the heat transferred between the solid and gas phases. The density and heat capacity are evaluated for the mixture of Mn_2O_3 and Mn_3O_4 based on the degree of conversion. Equation (8) is similar to the equation used by other authors,[12] except for the additional term $\dot{Q}_{rxn}$ that acts as a source term accounting for the heat involved in the chemical reaction. The heat transferred between the solids and the air is calculated from

$$\dot{Q}_{s\to f} = \frac{\dot{m}_{f,in}}{V_{bed}} \int_{T_{f,in}}^{T_{f,out}} c_{p,f}\, dT = \rho_{f,in} \frac{u_{f,in}}{L_{bed}} \int_{T_{f,in}}^{T_s} c_{p,f}\, dT \tag{9}$$

where $\dot{m}_{f,in}$ is the mass flow rate of the air at the reactor inlet and V_{bed} is the total volume of the bed. Note that $\dot{Q}_{s\to f}$ is negative when heat is transferred from the air to the solids during charging. The heat released during the oxidation or absorbed during the reduction is obtained from

$$\dot{Q}_{rxn} = -\left(1-\varepsilon_{bed}\right)\left(1-\varepsilon_{p}\right)\rho_{s,\mathrm{Mn_3O_4}}\Delta w_{theor,ox}\frac{\Delta H_{rxn}}{M_{O_2}}\frac{dX_s}{dt} \tag{10}$$

where $\rho_{s,\mathrm{Mn_3O_4}}$ is the intrinsic material density of $\mathrm{Mn_3O_4}$, $\Delta w_{theor,ox}$ is the theoretical relative weight gain during oxidation, ΔH_{rxn} is the heat of reaction per mole of oxygen, M_{O_2} is the molar weight of oxygen, and dX_s/dt is the conversion rate given by Eq. (2). The results obtained with the fluidized bed model are independent of the cross-sectional area of the reactor since Eq. (8) is formulated as a volumetric conservation equation and the reactor walls are assumed to be adiabatic. Furthermore, the results are independent of the particle size, but it should be kept in mind that the particles must be small enough for the assumption $T_{f,out} = T_s$ to hold, see Eq. (5) and Fig. 6. Equations (8)-(10) are solved consecutively with the implicit Euler method at each time step to a convergence tolerance of 10^{-8}.

References

1 L. Geissbühler, Master Thesis, ETH Zürich, 2014.

2 F. Pestalozzi, Master Thesis, ETH Zürich, 2013.

3 C. Bousquet-Berthelin and D. Stuerga, *J. Mater. Sci.*, 2005, **40**, 253 – 255.

4 K. T. Jacob, A. Kumar, G. Rajitha and Y. Waseda, *High Temp. Mater. Processes*, 2011, **30**, 459–472.

5 P. W. Atkins and J. De Paula, *Atkin's Physical Chemistry*, Oxford University Press, Oxford; New York, 10th edn., 2014.

6 D. Kunii and O. Levenspiel, *Fluidization Engineering*, Butterworth-Heinemann Boston, 2nd edn., 1991.

7 H. F. Rase, *Fixed-bed reactor design and diagnostics: gas-phase reactions*, Butterworth-Heinemann Boston, 1990.

8 J. González-Aguilar, *Personal Communication*, 2014.

9 E. W. Lemmon, M. O. McLinden and D. G. Friend, in *NIST Chemistry WebBook, NIST Standard Reference Database Number 69*, eds. P. J. Linstrom and W. G. Mallard, National Institute of Standards and Technology, Gaithersburg MD, 2011.

10 W. Yang, *Handbook of Fluidization and Fluid-Particle Systems*, CRC Press, 2003.

11 K. M. Wagialla, A. H. Fakeeha, S. S. E. H. Elnashaie and A. Y. Almaktary, *Energy Sources*, 1991, **13**, 189–201.

12 O. Levenspiel, *Engineering Flow and Heat Exchange*, Springer US, 3rd edn., 2014.